# Coarsening of unstable thin films subject to gravity

M. B. Gratton*
*Department of Mathematics, Duke University, Box 90320, Durham, North Carolina 27708-0320, USA*

T. P. Witelski†
*Oxford Centre for Industrial and Applied Mathematics, University of Oxford, 24-29 St Giles, Oxford OX1 3LB, United Kingdom*

(Received 9 July 2007; revised manuscript received 25 October 2007; published 4 January 2008)

Thin films of viscous fluids coating hydrophobic substrates are unstable to dewetting instabilities, and long-time evolution leads to the formation of an array of near-equilibrium droplets connected by ultrathin fluid layers. In the absence of gravity, previous use of lubrication theory has shown that coarsening dynamics will ensue—the system will evolve by successively eliminating small drops to yield fewer larger drops. While gravity has only a weak influence on the initial thin film, we show that it has a significant influence on the later stages of the coarsening dynamics, dramatically slowing the rate of coarsening for large drops. Small drops are relatively unaffected, but as coarsening progresses, these aggregate into larger drops whose shape and dynamics are dominated by gravity. The change in the mean drop shape causes a corresponding gradual transition from power-law coarsening to a logarithmic behavior.

DOI: 10.1103/PhysRevE.77.016301 PACS number(s): 47.20.Ma, 68.15.+e, 68.55.−a

## I. INTRODUCTION

Thin layers of viscous fluids on hydrophobic solid substrates experience instabilities that drive flat films to "dewet" into collections of droplets. These instabilities are tied to intermolecular forces between the fluid and the substrate [1,2] causing perturbations in the film to deepen [3,4] and grow into holes. Subsequently, the fluid reassembles into localized droplets [5]. In many problems other short-range forces produce an ultrathin film (UTF) adsorbed on the substrate, and the drops sit on top of this fluid layer. These drops are only metastable; they slowly communicate with neighbors by exchanging mass through the UTF. On very large time scales, this exchange leads to a coarsening in the number of drops, where smaller drops are drained through the UTF into their larger neighbors.

While the early stages of dewetting and film rupture have been extensively studied analytically [2–4,6], and experimentally [7–11], the later stages of coarsening has recently become the focus of extended numerical simulations and theoretical research. In [12,13] it was observed that the total number of drops in an idealized one-dimensional macroscopic system obeys a power law,

$$N(t) \propto t^{-2/5}, \tag{1.1}$$

which has been confirmed analytically by [14] and has been compared against results from experiments [15]. In this model, all drops were shown to have a particular parabolic profile that scales with their mass, but always retain the same apparent contact angle. In the early stages of evolution, the heights of these drops will be comparable to the initial film height. In many applications, the influence of gravity on this scale is negligible. For later stages of coarsening the fluid mass becomes segregated into smaller numbers of large drops. If the length scale of the system is large enough and sufficient (possibly quite long) time is allowed, the resulting coarsened drops may become considerably larger than the original height scale. In this limiting regime, the influence of gravity will come into effect causing the drops to deviate from the self-similar parabolic profile and flatten into "puddles" or "pancakes" [16–19]. Determining how this should modify the long-time coarsening behavior predicted by Eq. (1.1) is the theoretical motivation of this study.

We will show that incorporating the initially weak influence of gravity causes the coarsening drops to eventually to flatten in shape. This will be shown to lead to a crossover from power-law coarsening (1.1) to a logarithmic behavior. To our knowledge this dynamic transition has not been previously studied in detail. While the time scales involved in coarsening for some very thin dewetting films [7,9,20] may prove prohibitively long for experimental studies, many recent articles have considered the influence of gravity or similar forces on dewetting and thin film breakup [19,21–25] and work on dewetting in two-layer thin films has tentatively observed a transition in long-time coarsening dynamics [26].

The Navier-Stokes equations of fluid motion for incompressible thin films with long wavelength disturbances can be simplified under the lubrication approximation for low Reynolds number flows. This yields a partial differential equation for $h(x,t)$, the height of the film [2]. This reduction relies on a small aspect ratio of typical height scale to typical length scale, and on linearizing the mean curvature of the free surface, $\kappa \sim \nabla^2 h$. Analysis [14] and computation [14,23] for the full two-dimensional problem are very challenging current questions; in order to make progress in the current work, we restrict our attention to the simpler case of a one-dimensional height profile. The leading order model is the Reynolds lubrication equation

$$3\mu \partial_t h = \partial_x (h^3 \partial_x p), \tag{1.2}$$

where $\mu$ is the viscosity and the hydrodynamic pressure $p(x,t)$ is set by the sum of relevant forces,

*mgratton@math.duke.edu
†witelski@maths.ox.ac.uk

 

$$p = \Pi(h) - \gamma \partial_{xx} h + \rho g h, \tag{1.3}$$

where $\gamma$ is the fluid's surface tension, $\rho$ the density, and $g$ is the acceleration due to gravity. The disjoining pressure $\Pi(h)$ models the intermolecular forces, and we choose to use the form

$$\Pi(h) = \frac{A}{h^3}\left[1 - \frac{h_{\mathrm{UTF}}}{h}\right], \tag{1.4}$$

for the disjoining and/or conjoining intermolecular forces [2,12,13,27–31], where $h_{\mathrm{UTF}}$ sets the approximate height of the adsorbed ultrathin film and $A$ is the Hamaker constant. Coarsening experiments performed in [15] used for polystyrene on SiO, where $h_{\mathrm{UTF}} \approx 1.3$ nm and $A \approx 2 \times 10^{-20}$ J [32]. Similar forms of $\Pi(h)$ have been used to represent the Lenard-Jones 6–12 potential, and other functional forms produce similar results [22,24]. However, $\Pi(h)$ will have important qualitative differences for describing other physical regimes [33].

We nondimensionalize Eq. (1.2) by introducing scales

$$h = H\hat{h}, \quad x = L\hat{x}, \quad t = T\hat{t}, \quad h_{\mathrm{UTF}} = H\delta,$$

where $\delta$ represents the height of the UTF relative to a typical film height, $\delta = (h_{\mathrm{UTF}}/H) < 1$. $H$ is the thickness of the initial unstable film layer, which can be in the range $H \approx 10 - 300$ nm [32]. We pick the length scale to balance the influence of surface tension and the disjoining pressure, $L = H\sqrt{\Xi}$, where $\Xi$ is the dimensionless ratio

$$\Xi = \gamma h_{\mathrm{UTF}}^2 / A, \tag{1.5}$$

with $\Xi \approx 10$ for polystyrene on SiO. Length scale $L$ is comparable to the "healing length" [34] and [18, Chap. 4], also called the cicatrization length [35]. It is the appropriate scale for describing small droplets and other structures produced by spinodal dewetting, typically $L = O(\mu\mathrm{m})$.

There is another length scale in this problem, obtained by balancing surface tension and gravity—this is the capillary length, $\ell_c = \sqrt{\gamma/\rho g}$, and it is much larger, typically $O(\mathrm{mm})$. It is too large for describing the early to moderate structures formed in this system, but we will see that it will become the dominant scale for the dynamics at very long times.

As usual in lubrication models, the time scale scales with the viscosity, $T = 3\mu H \Xi^2/\gamma \approx 10^{-2}$ s. While the initial stages of dewetting happen on this fast time scale, coarsening is a quasisteady process, and as we will see, very long times will be involved for the complete dynamics (days, months, or longer). Dropping the hats for convenience, we obtain the dimensionless equation

$$\frac{\partial h}{\partial t} = \frac{\partial}{\partial x}\left[h^3 \frac{\partial}{\partial x}\left(f(h) - \frac{\partial^2 h}{\partial x^2} + \alpha h\right)\right]. \tag{1.6}$$

The function $f(h)$ is the nondimensional form of $\Pi$,

$$f(h) = \frac{\delta^2}{h^3}\left[1 - \frac{\delta}{h}\right], \tag{1.7}$$

where the factor of $\delta^2$ is included so that the apparent contact angle of the resulting partially wetting drops is fixed in the limit $\delta \to 0$ [12,36].

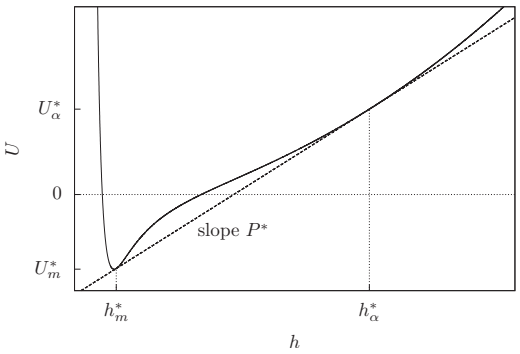


FIG. 1. The generalized wetting potential $U(h)$, incorporating contributions for both intermolecular forces and gravitational forces. The dashed line shows the double tangent of slope $P^*$ meeting the potential at values $h_m^*$ and $h_\alpha^*$.

The only remaining parameter in Eq. (1.6) is the ratio of the influence of gravity compared with the disjoining pressure, which can be expressed as

$$\alpha = \frac{\rho g H^4 \delta^2}{A} = \frac{\rho g H^2 \Xi}{\gamma} = (H/\ell_c)^2 \Xi. \tag{1.8}$$

For dewetting polymer films $\alpha \approx 10^{-9} - 10^{-7}$, but given a sufficiently large total fluid mass in an experimental system, coarsening will eventually produce large drops with heights $\gg H$ for which gravity is dominant. In [22] it is remarked that while $\alpha$ may be small it has an important influence on the problem that cannot be neglected for the long-term behavior. In other classes of dewetting problems studies have suggested that the influence of gravity plays a more immediate role and correspond to larger values of $\alpha \sim 10^{-3} - O(1)$ [23,26].

It is convenient to combine the effects of gravitational hydrostatic pressure, $\alpha h$, and intermolecular forces, $f(h)$, into one *generalized wetting potential* $U(h)$,

$$U(h) = -\frac{\delta^2}{h^2}\left(\frac{1}{2} - \frac{\delta}{3h}\right) + \frac{1}{2}\alpha h^2, \tag{1.9}$$

shown in Fig. 1 with

$$U'(h) = f(h) + \alpha h; \tag{1.10}$$

see Fig. 2. Then the final form of the dimensionless pressure is

$$p = -\partial_{xx} h + U'(h), \tag{1.11}$$

the mass flux is

$$J = -h^3 \partial_x p, \tag{1.12}$$

and the governing partial differentail equation (PDE) can be written as

$$\frac{\partial h}{\partial t} = -\frac{\partial}{\partial x}\left[h^3 \frac{\partial}{\partial x}\left(\frac{\partial^2 h}{\partial x^2} - U'(h)\right)\right]. \tag{1.13}$$

The wetting potential is a nonconvex, double-welled potential and correspondingly $U'(h)$ is nonmonotone. Similar potentials have been considered by others [22,24,28,29]. Al-

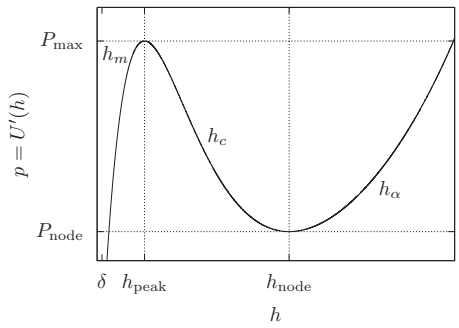


FIG. 2. The derivative of the generalized wetting potential, $U'(h)=f(h)+\alpha h$, with $h$ plotted on a logarithmic scale. Dotted lines separate the three branches of fixed points $\{h_m,h_c,h_\alpha\}$ discussed in Sec. II.

gebraic calculations show this structure for Eq. (1.9) holds as long as $\alpha \ll \delta^{-2}$. For $h$ near $\delta$ the potential is controlled by the conjoining and disjoining intermolecular forces. For larger heights, $h \gg \delta$, gravity is the dominant factor and the potential would be significantly different without it [22]. Equation (1.13) is a form of the Cahn-Hilliard equation, modeling phase separation between two energetically favorable states. In connection with thin films, this phase separation is called spinodal dewetting [2,9,10], with the preferred states being droplets and the UTF.

We investigate the long-time dynamics of Eq. (1.13) by adapting the approach used in [12,13] for coarsening of dewetting thin films. The PDE can be reduced to a low-dimensional system for the coupled behavior of an array of near-equilibrium drops parametrized by their positions and pressures. Ordinary differential equations (ODEs) are obtained by linearizing about a representative steady-state droplet solution $h(x-X;P)$ and projecting onto the eigenfunctions of the adjoint linearized operator to yield

$$\frac{dP_i}{dt} = C_p(P_i)(J_{i+1,i} - J_{i,i-1}),$$

$$\frac{dX_i}{dt} = -C_x(P_i)(J_{i+1,i} + J_{i,i-1}). \tag{1.14}$$

Here, $C_p$ is a mass-exchange coefficient controlling how fast drops grow or shrink and $C_x$ is a drift-coefficient controlling how fast drops move. The fluxes $J_{i,i-1}$ between adjacent drops are computed between drops through a quasistatic approximation. These equations are supplemented by "coarsening rules" [37] that describe how to resume the evolution of the droplet array after any brief far-from-equilibrium dynamics connected to finite-time singular behavior of Eq. (1.14) when droplets disappear from the system. The number of drops decreases through one of two possible mechanisms: (i) if contact lines of drops collide, then the drops merge together (a "collision" event), or (ii) if fluxes through the UTF reduce a droplet's mass below a critical level, it collapses into the UTF mean field (a "collapse" event). Equations (1.14) and the coarsening rules together define a "coarsening dynamical system" (CDS) [38] that describes the evolution of a set of drops as more and more successively coarsen out.

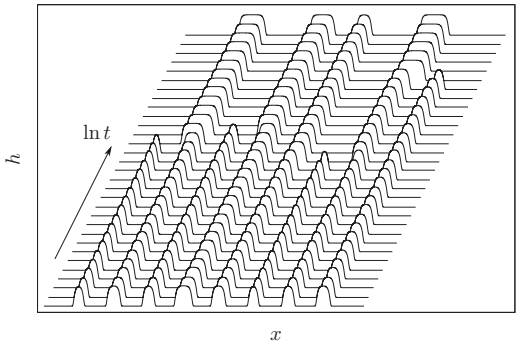


FIG. 3. Numerical simulation of a small array of interacting drops in Eq. (1.13). The array coarsens over long time scales. Small parabolic drops generally decrease in mass until they collapse, while larger drops become mesalike in shape.

After the short-time rupture and dewetting instabilities have produced a large array of droplets, the coarsening mechanisms force the number of drops, $N(t)$, to be a steadily decreasing function of time. For very large droplet arrays, analysis of $N(t)$ is the simplest measure that can yield insight on the complex dynamics of the system. We will show how the presence of gravity influences the coarsening dynamics of dewetting thin films by describing the differences from the previously known coarsening rate law in absence of gravity (1.1). Figure 3 shows a computation for Eq. (1.13) with an illustrative value of $\alpha$ and an initial array of eight drops. As time progresses, large drops become larger and more mesalike, while small drops become smaller and more parabolic, eventually melting into the UTF. We proceed as follows. First, we map out the form of steady-state droplets of Eq. (1.13) in Sec. II. We then generalize the CDS model to the new structure of the family of droplets in Sec. III. We examine the results of these numerical simulations of the CDS in Sec. IV and give a prediction for the coarsening law.

## II. STEADY-STATE DROPLET SOLUTIONS

We briefly review the analysis for equilibrium partially-wetting drop profiles in one dimension, as has been presented in [16, Sec. D2] and others [5,18,22]. Equation (1.13) has a monotone decreasing energy functional,

$$E = \int U(h) + \frac{1}{2}h_x^2 dx,$$

$$\frac{dE}{dt} = -\int h^3 p_x^2 dx \leqslant 0. \tag{2.1}$$

Nontrivial equilibria are stationary points of the energy and must have constant pressure, $p \equiv P$. Steady state solutions are then given by the solutions of the differential equation

$$\frac{d^2h}{dx^2} = U'(h) - P. \tag{2.2}$$

Relevant bounded-in-height solutions of this equation can exist only for the pressures $P_{\text{node}} < P < P_{\max}$. This range cor-

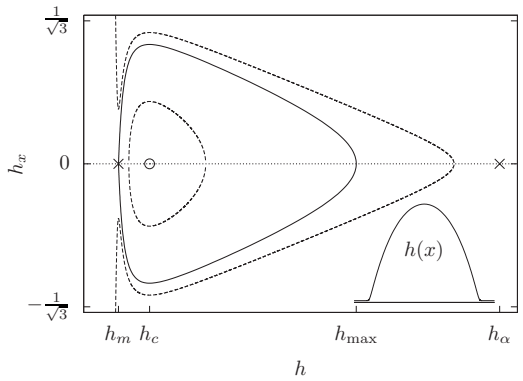


FIG. 4. Phase plane for $P^* \ll P < P_{\max}$. The inset shows the parabolic drop profile $h(x)$ corresponding to the homoclinic orbit.

responds to the range of heights where a uniform film is linearly unstable, $h_{\text{peak}} < h < h_{\text{node}}$, [5,22]. In this pressure range, Eq. (2.2) has three fixed points, $\{h_m, h_c, h_\alpha\}$, given by the roots of

$$U'(h) = P, \tag{2.3}$$

see Fig. 2. For the potential (1.9) these fixed points for $\delta \to 0$ are approximated by

$$h_m = \delta + \delta^2 P + \delta^3(4P^2 - \alpha) + O(\delta^4),$$

$$h_c = \frac{1}{P^{1/3}}\delta^{2/3} - \frac{1}{3}\delta + \delta^{4/3}\left(\frac{2}{9}P^{1/3} - \frac{\alpha}{3P^{5/3}}\right) + O(\delta^{5/3}),$$

$$h_\alpha = \frac{P}{\alpha} + O(\delta^2). \tag{2.4}$$

$h_c$ and $h_\alpha$ depend on the pressure at leading order while the nominal UTF thickness, $h_m$, has a weaker dependence. In the phase plane for Eq. (2.2) $h_m$ and $h_\alpha$ are saddle points, while $h_c$ is a center, see Fig. 4. At $P_{\text{node}}$ and $P_{\max}$, saddle-node bifurcations occur with the coalescence of $h_c$ and either $h_m$ or $h_\alpha$, respectively, as seen in Fig. 2.

Finite mass fluid droplets are given by solutions that are homoclinic to $h_m$. Such solutions exist for each pressure in the range $P^* < P < P_{\max}$, see Figs. 4 and 5. Here $P^*$ is a critical value of the pressure where a saddle-saddle heteroclinic orbit exists between $h_m$ and $h_\alpha$; below $P^*$ solutions describe localized "dimple" perturbations to uniform films. This structure for the set of equilibrium solutions was found in [22]. This pressure is set by the slope of the double tangent line to $U(h)$, as seen in Fig. 1, and satisfies the set of equations

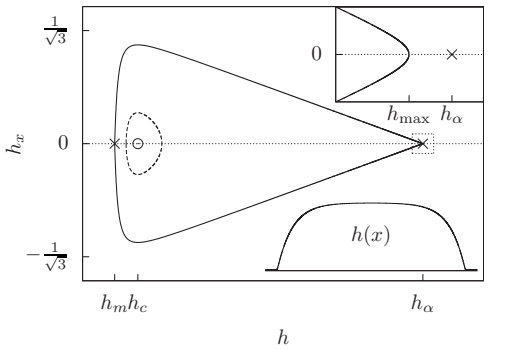


FIG. 5. Phase plane for $P \gtrsim P^*$. Note that the homoclinic orbit passes through $h_m$ and very near $h_\alpha$ (see top inset). The bottom inset shows the corresponding mesalike drop profile $h(x)$.

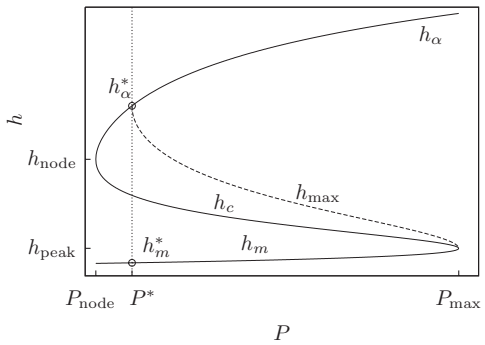


FIG. 6. The bifurcation diagram for fixed points $\{h_m, h_c, h_\alpha\}$ of Eq. (2.2), shown as solid curves. The dashed curve shows the value of $h_{\max}$. Note $h$ is plotted on a logarithmic scale. Droplet solutions exist for $P^* < P < P_{\max}$.

$$U(h_\alpha^*) - U(h_m^*) = (h_\alpha^* - h_m^*)P^*,$$

$$U'(h_m^*) = U'(h_\alpha^*) = P^*, \tag{2.5}$$

where $h_m^*, h_\alpha^*$ are the values of $h_m, h_\alpha$ at $P^*$. This is similar to the double tangent construction shown in [18, Fig. 7.3]. These quantities are approximately

$$P^* = \sqrt{\alpha/3} + \delta\alpha + O(\delta^2),$$

$$h_m^* = \delta + \delta^2\sqrt{\alpha/3} + \delta^3\frac{4}{3}\alpha + O(\delta^4),$$

$$h_\alpha^* = (3\alpha)^{-1/2} + \delta + O(\delta^2). \tag{2.6}$$

Equation (2.2) has a first integral giving droplet profiles passing through $h_m$ as

$$\frac{dh}{dx} = \pm r(h),$$

$$r(h) = \sqrt{2[U(h) - U(h_m) + P(h_m - h)]}. \tag{2.7}$$

The maximum height of a drop, $h_{\max}$, is the $O(1)$ root of $r(h_{\max}) = 0$. In the limit $\delta \to 0$, we find

$$h_{\max} = \frac{P - \sqrt{P^2 - \alpha/3}}{\alpha} + \frac{\delta P}{\sqrt{P^2 - \alpha/3}} + O(\delta^2). \tag{2.8}$$

We note that the droplet maximum is always bounded from above by $h_\alpha$ and as $P \to P^*$, $h_{\max} \to h_\alpha$, see Fig. 6. The values $h_m^*, h_\alpha^*$ give uniform lower and upper bounds for the heights of all possible droplets, respectively. We will later show that $h_\alpha^*$ corresponds to known results for heights of very large drops [18].

Two basic drop properties, the mass and width, may be found by integrating in the phase plane using Eq. (2.7). The drop mass $m$, or volume, is given by

$$m(P) = 2\int_{h_m}^{h_{\max}} \frac{h - h_m}{r(h;P)} dh, \tag{2.9}$$

where we subtract the UTF contribution as it is adsorbed to the substrate. To define an effective droplet width we use the position where $h=h_{\text{peak}}$; this value corresponds to the maximum of $U'(h)$ gives an effective dividing line between the edge of the droplet core and the outer UTF [5], leading to the expression for the width,

$$w(P) = \int_{h_{\text{peak}}}^{h_{\max}} \frac{1}{r(h;P)} dh. \tag{2.10}$$

In general, $m$ and $w$ must be found numerically. For the two special cases of large and small drops, we can additionally describe these drop properties through asymptotic expressions.

The case of small drops, given by the $\alpha \to 0$ limit, is identical to the analysis in [12,13]: (i) the lower bound on pressures goes to zero, $P^* \to 0$ and (ii) the upper bound on heights diverges, $h_\alpha \to \infty$. In [12] it was shown that for $\alpha = 0$, all drops have a parabolic profile in the their "core" region, where $h \gg \delta$ and surface tension dominates intermolecular forces,

$$h(x) \sim \frac{1}{2} P(w^2 - x^2), \quad |x| < w. \tag{2.11}$$

Asymptotic matching of the core to the outer UTF (where intermolecular forces dominate) through a contact line layer determined the droplet width to be $w \sim 1/(\sqrt{3}P)$. The core of those droplets can be integrated to yield the mass

$$m(P) = \int_{-w}^{w} h(x) - h_m dx \sim \frac{2\sqrt{3}}{27P^2}. \tag{2.12}$$

From Eq. (2.11) the maximum height is $h_{\max} = \frac{1}{2}Pw^2 \sim 1/(6P)$. Correspondingly we note that the $\alpha \to 0$ limit of Eq. (2.8) is also $1/(6P)$. By examining Eq. (2.8) we deduce that the regime of small mass (i.e., large pressure) droplets in Eq. (2.2) can be defined by the condition

$$P \gg \sqrt{\alpha}. \tag{2.13}$$

As expected, gravity has a weaker influence than surface tension and the disjoining pressure for small droplets. Hence Eq. (2.11) remains a good description of droplets with pressures in the range $\sqrt{\alpha} \ll P \leqslant P_{\max}$, see Fig. 4.

Our focus turns to the structure of very large drops, where gravity comes into play. Droplets of arbitrarily large masses are possible, the definition of large vs. small masses has to be given relative to $\alpha$, see Eq. (2.13). Since their height is strictly bounded by $h_\alpha^*$, they take the form of wide, flat "mesas" or "puddles" [17–19], see Fig. 5. In this context, we will find it more convenient to distinguish drops as being parabolic or mesalike, rather than large or small. For mesalike drops, the homoclinic orbit passes very near the $h_\alpha$ saddle point resulting in a long region where the height is nearly constant. Note that $h_\alpha > h_{\text{node}}$, so locally, the cores of mesa drops are in the linearly stable range of film heights.

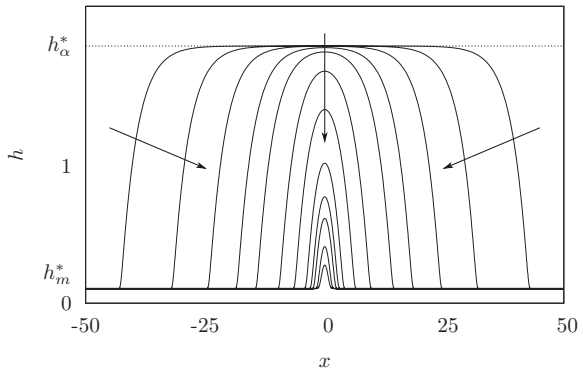


FIG. 7. Drop profiles for $\alpha=0.1$ and different pressures $P^* < P < P_{\max}$. The arrows show the trend for increasing pressure. Larger drops ($P \to P^*$) have $h_{\max} \approx h_\alpha^*$ and a mesalike shape, while smaller drops ($P \to P_{\max}$) approach a more parabolic structure.

Figure 7 shows the family of drops at a fixed value of $\alpha$ with the pressure being increased over the range $P^* < P < P_{\max}$. Figure 8 shows a series of drop profiles with mass fixed as the relative influence of gravity is increased. The contact angle for our drops in the small mass limit is given analytically by $\tan\theta \sim (H/L)h_x(-w) \sim \sqrt{A/(3\gamma h_{\text{UTF}}^2)}$ by a procedure given in [12], yielding the fixed angle

$$\theta \sim 1/\sqrt{3\Xi}. \tag{2.14}$$

This angle is independent of $\delta$ through our scaling of Eq. (1.7). As can be seen from Figs. 7 and 8, the contact angle of drops is independent of gravity and droplet size. This is as expected since the contact angle is determined by a balance of surface tension and the disjoining pressure at the contact line.

The structure of large drops is most easily examined by considering the $P \to P^*$ limit. Some droplet properties can be obtained as regular perturbation expansions,

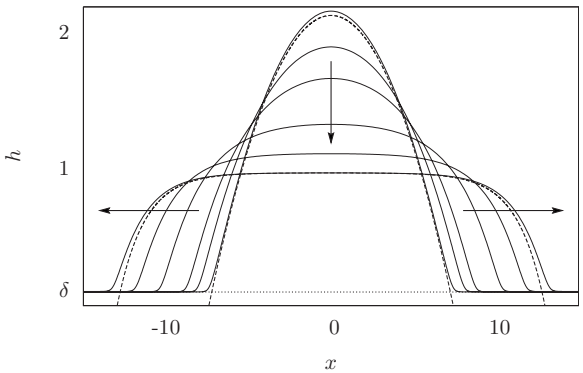


FIG. 8. Drop profiles for mass $m=20$ and $0 \leqslant \alpha \leqslant 0.4$. The drops become shorter and wider as $\alpha$ increases, shown by the arrows. The dashed profiles are the asymptotic approximations to the $\alpha=0$ and the $\alpha=0.4$ drops from Eqs. (2.11) and (2.17), respectively.

$$h_m = h_m^* + \frac{P - P^*}{U''(h_m^*)} + O([P - P^*]^2),$$

$$h_\alpha = h_\alpha^* + \frac{P - P^*}{U''(h_\alpha^*)} + O([P - P^*]^2),$$

$$h_{\max} = h_\alpha^* - \beta^* \sqrt{P - P^*} + O(P - P^*), \tag{2.15}$$

where

$$\beta^* = \sqrt{\frac{2(h_\alpha^* - h_m^*)}{U''(h_\alpha^*)}} \sim \left(\frac{4}{3\alpha^3}\right)^{1/4}.$$

In this limit, the height profile approaches the heteroclinic trajectory connecting $h_m^*$ to $h_\alpha^*$, see Fig. 5. Comparing the eigenvalues of the two saddles, $\lambda = \pm\sqrt{U''(h)}$, of Eq. (2.2) reveals that $(\lambda_m^* \approx 1/\delta) \gg (\lambda_\alpha^* \approx \sqrt{\alpha})$, so the form of the solutions will be dominated by the behavior near $h_\alpha$. Linearizing (2.2) about $h_\alpha$ gives

$$\frac{d^2h}{dx^2} \sim U''(h_\alpha)(h - h_\alpha), \tag{2.16}$$

where we assume that $h_\alpha - h_{\max}$ is small. Solving this equation subject to $h(0) = h_{\max}$ and $h'(0) = 0$ gives

$$h \sim [h_\alpha - (h_\alpha - h_{\max})\cosh(x\sqrt{U''(h_\alpha)})]_+, \tag{2.17}$$

see Fig. 8. The edge of the region of support for this linearized solution gives a good estimate for the width of drops, $h(w) = 0$,

$$w = \frac{1}{\sqrt{U''(h_\alpha)}} \operatorname{arccosh}\left(\frac{h_\alpha}{h_\alpha - h_{\max}}\right), \tag{2.18}$$

while the detailed structure near the contact line involves further matched asymptotics [17]. We then approximate the drop mass by

$$m = \int_{-w}^{w} h(x) - h_m dx = 2\left((h_\alpha - h_m)w - \frac{h_\alpha - h_{\max}}{\sqrt{U''(h_\alpha)}} \sinh[w\sqrt{U''(h_\alpha)}]\right). \tag{2.19}$$

To explicitly describe the sensitive dependence of the drop mass and width on the pressure, it is convenient to define a new parameter, *log excess pressure*

$$Q = \ln(P - P^*), \tag{2.20}$$

with $Q \to -\infty$ corresponding to $P \to P^*$. Expanding $w$ and $m$ gives

$$w(Q) \sim \frac{1}{\lambda_\alpha^*} \ln\left(\frac{2h_\alpha^*}{\beta^*}\right) - \frac{Q}{2\lambda_\alpha^*}, \tag{2.21a}$$

and

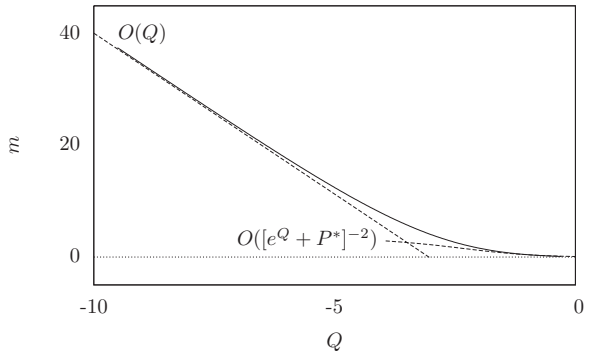


FIG. 9. The $m$ to $Q$ relationship for $\alpha = 0.1$. Dashed lines show the estimates (2.21b) for large drops and Eq. (2.11) for small drops.

$$m(Q) \sim \lambda_\alpha^* \beta^{*2} \ln\left(\frac{2h_\alpha^*}{\beta^*}\right) - \frac{2h_\alpha^*}{\lambda_\alpha^*} - \frac{1}{2}\lambda_\alpha^* \beta^{*2} Q \sim \frac{1}{\alpha\sqrt{3}}\left(-Q + \frac{1}{2}\ln\alpha\right). \tag{2.21b}$$

Figure 9 shows the numerically computed mass of drops as a function of pressure compared against the low-mass and high-mass limits, Eqs. (2.12) and (2.21b), respectively.

The $Q \to -\infty$ limit corresponds to the heavy drops analyzed in [18, chap. 2]. We can relate $h_\alpha^*$ to the expression for the dimensional value of the height of puddle drops with small contact angle $\theta$,

$$e = 2\sqrt{\gamma/\rho g}\,\sin(\theta/2) \sim \ell_c \theta. \tag{2.22}$$

Using Eq. (2.6) for $h_\alpha^*$ with Eqs. (2.14) and (1.8) yields

$$H h_\alpha^* \sim \frac{H}{\sqrt{3\Xi(H/\ell_c)^2}} = \ell_c \theta, \tag{2.23}$$

corresponding exactly with $e$ showing that our analysis is consistent with the previous studies of large equilibrium drops.

Returning to our analysis, we see that by combining (2.21b) with Eq. (2.13) a drop is well approximated by the pancake profile (2.17) when its *mesa parameter* is large,

$$\mathbb{M} \equiv m\alpha \gg 1. \tag{2.24}$$

This condition provides an effective dividing line between parabolic and mesa drop behaviors that will be useful later.

## III. QUASISTATIC MODEL FOR LONG-TIME BEHAVIOR

Multidrop systems exist as combinations of near-equilibrium individual droplets, each close to equilibrium locally, though the system is far from equilibrium globally. Neighboring drops with different masses have different equilibrium pressures and corresponding UTF heights. Though these differences are only $O(\delta^2)$, see Eq. (2.4), the corresponding differences in the pressure drives the evolution, as equilibrium cannot occur until $p$ has the same value everywhere. In the UTF region, the film has height $O(\delta)$, and so

the evolution occurs on long time scales that are $O(1/\delta^3)$, as the flux scales similar to $O(h^3)$.

The long time scale associated with the fluxes motivates a quasistatic model for the evolution of drops. Following the analysis of [12,13], we reduce the PDE problem into a CDS consisting of coupled ODEs for slow processes and rules for isolated fast, far-from-equilibrium events occurring when the solutions of the slow-time ODEs yields singularities. These rules approximate the fast dynamics and return the model to a quasistatic state. This approach locally linearizes about each of an array of $N$ steady-state drops parametrized by their positions $X_i$ and their logarithmic excess pressures $Q_i$, $h \sim h[x - X_i(t); Q_i(t)]$ for $i = 1, 2, \ldots, N$. Between drops, the pressure has a constant gradient between the flat states corresponding to droplet cores. Rescaling Eq. (1.13) for heights of $O(\delta)$ shows that the UTF height evolves slowly, slaved to the behavior of the adjoining drops. The UTF serves to couple adjacent drops by allowing a flux between them, which is given by Eq. (1.12). The pressure is dominated by the intermolecular forces, so $p \sim U'(h)$. This gives $J = -h^3 U''(h)\partial_x h$. It is convenient to express this as the derivative of a chemical potential-type function, $J = -\partial_x V(h)$, where

$$V(h) = \int^h s^3 U''(s) ds = -3\delta^2 \ln(h) - 4\delta^3/h + \alpha h^4/4. \tag{3.1}$$

Finally, since the pressure gradient is nearly constant between drops, we approximate the derivative of $V(h)$ with the difference of the values of $V$ at the edges of neighboring drops. The flux between drop $i$ and $i+1$ is then

$$J_{i,i+1} = -\frac{V(h_m(Q_{i+1})) - V(h_m(Q_i))}{[X_{i+1} - w(Q_{i+1})] - [X_i + w(Q_i)]}. \tag{3.2}$$

ODEs for $X_i$ and $Q_i$ can be found by forming the next-order equation in the linearization and finding the eigenfunctions of the adjoint operator. Projecting this equation onto the eigenfunctions gives

$$\frac{dQ_i}{dt} = C_q(Q_i)(J_{i+1,i} - J_{i,i-1}), \tag{3.3a}$$

$$\frac{dX_i}{dt} = -C_x(Q_i)(J_{i+1,i} + J_{i,i-1}), \tag{3.3b}$$

where $C_q$ is the mass-exchange coefficient

$$C_q(Q) = \left( \int_{-w}^{w} \partial_Q h \, dx \right)^{-1}, \tag{3.4}$$

and $C_x$ is the drift coefficient

$$C_x(Q) = \frac{\int_{-w}^{w} [(h - h_m)/h^3] dx}{2\int_{-w}^{w} [(h - h_m)^2/h^3] dx}. \tag{3.5}$$

Equations (3.3a) and (3.3b) describe the slow evolution of interacting drops. The solutions of these equations can become singular in finite time when Eq. (3.2) diverges, producing coarsening events. The numerator may diverge if $V$ diverges. This occurs when $Q_i > Q_{\max}$, where $Q_{\max} = \ln(P_{\max} - P^*)$, as the pressure has moved out of the acceptable range for drop steady states, in an event we will call a *collapse*. In fact, the evolution of such drops becomes rapid when $Q > Q_{\text{fast}}$, where $Q_{\text{fast}}$ is the global minimum of $C_q$ as seen in Fig. 10.

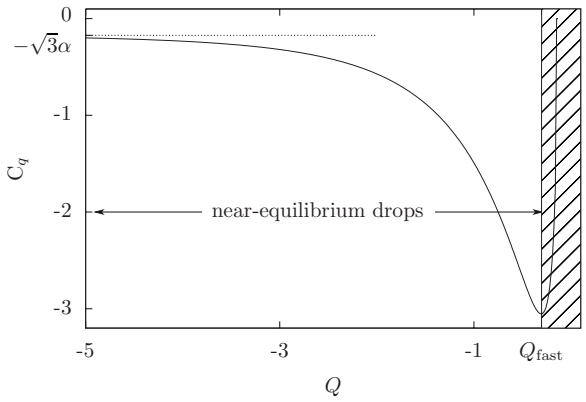


FIG. 10. $C_q(q)$ for $\alpha = 0.1$. Estimate Eq. (3.6) gives the $Q \to -\infty$ limit, shown dotted. The minimum value, $Q_{\text{fast}}$ is the boundary between near-equilibrium drops described by the quasistatic model and rapidly varying drops that are deleted (the shaded area). It is used as the criterion in our coarsening rule for determining collapse.

These small drops are no longer quasistatic, they melt rapidly into the UTF. We delete such drops and continue with the $N-1$ remaining drops. The amount of mass lost in this deletion is negligible. A second mechanism for Eq. (3.2) to diverge is for the denominator to go to zero, i.e., the contact lines of the two neighboring drops collide. This event, a *collision*, can be dealt with by a similar rule discussed in [13].

To compute solutions, we tabulate $h_m$ and $C_q$ for a range of $Q$ values. We find the minimum height by solving (2.3) for the $O(\delta)$ root. We can express $C_q$ by combining Eq. (3.4) with the basic statement of conservation of mass to see $C_q(Q) = (dm/dQ)^{-1}$. The drop mass and width are computed from the integrals in the phase plane (2.9) and (2.10). For $Q$ large and negative, computing the value $r(h; P)$ needed in these integrals becomes problematic due to $P$ being very close to $P^*$, and so tabulated quantities must be supplemented with the asymptotic relations for $h_m$, $m$, $w$, and $C_q$. The first three expansions appear in Sec. II, and we may use Eq. (2.21b) for $Q \to -\infty$ to give

$$C_q(Q) \sim -\sqrt{3}\alpha - \frac{1}{\sqrt{2}}(3\alpha^3)^{1/4} e^{Q/2}. \tag{3.6}$$

We will restrict attention to class of problems where the dominant form of coarsening events are collapses. This regime can be observed for small values of the reduced coarsening parameter [13],

$$\mathbb{K} \equiv \left( \frac{\bar{H}}{\delta} - 1 \right) < 1, \tag{3.7}$$

with $\bar{H} = M/L$ where $M$ is the total mass and $L$ the total length of the domain. The total mass can be separated into

the contribution from the UTF layer and the masses of the drop cores, $M=L\delta+M_c+O(\delta^2 L)$ where $M_c=\Sigma m(Q_i)$. Consequently, $\mathbb{K}$ gives the ratio of average drop to UTF mass which gives a measure of droplet density; small $\mathbb{K}$ describes a dilute system. For small $\mathbb{K}$ with $\alpha=0$ in [13], arguments using the form of the coefficient functions in Eqs. (3.3a) and (3.3b) showed that the positions of drops evolve slowly compared to their pressures. For $\alpha>0$ the $C_x$ function is qualitatively similar, and similar behavior is expected to hold. In our simulations, we take $\mathbb{K}\leqslant 1/2$ with equally-spaced drops and observe no collisions. In addition, the evolution of position is sufficiently slow so that the drift equations can be eliminated and only pressures simulated. This assumption will be checked in Sec. IV by computations, where we will study Eq. (3.3a) along with the rule for collapse as a model for droplet coarsening.

## IV. COARSENING RATES

Using the CDS described above we study how the behavior of $N(t)$ is effected by $\alpha$ and the average mass. The number of drops is a quantity that is easy to measure experimentally, and its behavior determines the scales for other evolving properties in the system. In particular, we start with $N_0$ initial drops in a domain of length $L$ with no-flux boundary conditions. The total core mass $M_c$ (and hence $\mathbb{K}$) is conserved to $O(\delta^2)$ throughout each simulation. Drops in the array are chosen to be initially equally-spaced and have mass randomly distributed about a mean,

$$X_i = i\ell \quad \text{and} \quad Q_i = Q(\mathcal{N}(\bar{m}_0,\sigma);\alpha), \tag{4.1}$$

for $i=1,2,3,\ldots,N_0$ and where $\ell=L/N_0$ and $Q(m;\alpha)$ is the inverse function that relates mass to logarithmic excess pressure found numerically from Eq. (2.9) with $\mathcal{N}(\bar{m},\sigma)$ being the normal distribution with mean $\bar{m}_0=M_c/N_0$ and standard deviation $\sigma$. Note that the coarsening parameter can be written as

$$\mathbb{K} = \frac{\bar{m}_0}{\ell\delta}.$$

These initial conditions give a reasonable approximation of the drops arising from the dewetting instability acting on a flat film. The details of the separation between drops due to dewetting can be found elsewhere [22].

For all computations shown here, we use an adaptive Runge-Kutta scheme and choose parameters $\delta=0.1$, $0<\alpha<0.5$, and $\mathbb{K}\leqslant 0.5$. With these parameters, the influence of the drift equations (3.3b) are negligible. Figure 11 shows the results of simulations with drift (dashed lines) and without drift (solid lines). In each run, $\bar{m}_0=1$, $\sigma=0.1$, and $\mathbb{K}=0.25$. The $\alpha=0.3$ runs use 2000 initial drops so that the two cases are graphically distinct. The onset time can be seen around $t=10^5$ and after this self-similar coarsening behavior sets in. For $\alpha=0$, the well-known power law (1.1) is observed across six decades of time. The variation between the model without drift (3.3a) and the full model (3.3) only becomes apparent as the number of drops becomes small. Even here, both curves still follow the same average trend, though with different variations. The $\alpha=0.3$ curve appears to follow the power law for times close to onset, but longer times show the rate slowing down. At $t=10^{12}$, there are some 60 drops remaining for $\alpha=0.3$, compared to only 2 for $\alpha=0$.

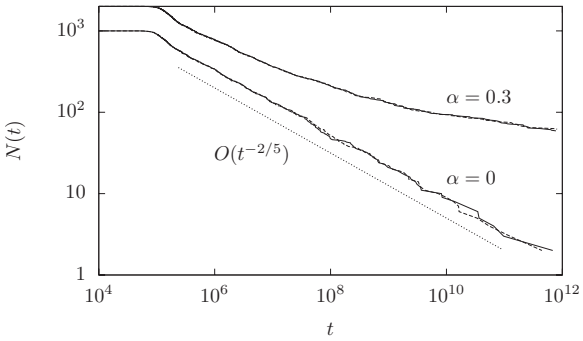


FIG. 11. The total number of drops $N$ versus $t$ for the model with drift (solid) without drift (dashed). The differences in the curves are more noticeable when $N$ is small. The dotted line shows the predicted power law for $\alpha=0$.

When $\alpha$ is positive, non-power-law behavior is clear for long times. The pressure dependence of the drop shape due to the presence of gravity causes a dramatic slow down in the coarsening rate. While the rate approaches a $t^{-2/5}$ power law when the drops are parabolic, it slows down as drops grow to become more mesalike (see Fig. 3). The effects of changing $\alpha$ over a range of values can be seen in Fig. 12, where we plot $N(t)$ on a log-log scale. To properly compare initial conditions, we use Eq. (4.1) in all simulations, with $\bar{m}_0=2$ and $\mathbb{K}=0.5$; for each $\alpha$ this yields a different range of $Q_i$ due to the form of Eq. (2.21b). The $\alpha=0$ curve follows power-law equation (1.1) to the end of the coarsening regime, but all of the $N(t)$ curves with $\alpha>0$ eventually deviate from this power-law. For the smallest value plotted, $\alpha=0.02$, the curve maintains the power-law for nearly seven decades, but then the coarsening rate eventually slows. For the largest value, $\alpha=0.5$, $N(t)$ slows from the power law almost immediately. The coarsening is quite slow; after $10^{40}$ units of time, nearly 1300 drops remain for $\alpha=0.5$, while the $\alpha=0$ system essentially reached steady-state 24 decades earlier.

In Fig. 13, several simulations with $\alpha=0.1$ and $N_0=10\,000$ show different onsets of the slower coarsening behavior tied to different values of the droplet initial mass,

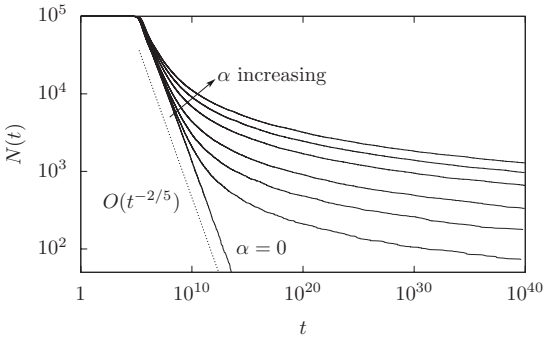


FIG. 12. The coarsening rate as modified by $\alpha$ for $0\leqslant\alpha\leqslant 0.4$. The results for $\alpha=0$ follow a $t^{-2/5}$ power-law behavior (dotted), different from the results for $\alpha>0$.

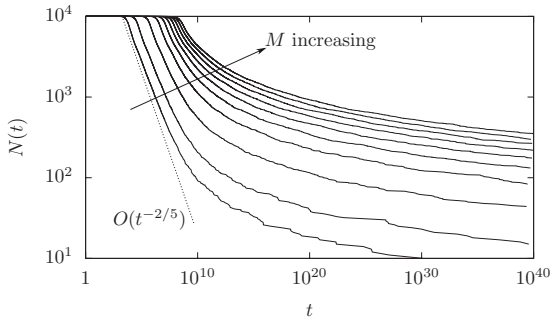


FIG. 13. The coarsening rate as effected by changing $\bar{m}_0$, with $0.5 \leqslant \bar{m}_0 \leqslant 20$ and fixed $\alpha = 0.1$.

$0.5 \leqslant \bar{m}_0 \leqslant 20$. The coarsening parameter is fixed at $\mathbb{K} = 1/5$ by varying $\ell$ in proportion to $\bar{m}_0$. For $\bar{m}_0 = 20$ and $\bar{m}_0 = 17.5$, the two largest values plotted, $\bar{\mathbb{M}} \gg 1$ and so the droplets are initially mesalike. The slower coarsening is in effect for these curves almost at the onset of the coarsening itself. For the smallest value of $\bar{m}_0$, drops are initially parabolic with $\bar{\mathbb{M}} = 1/20$, and the $N(t)$ curve can be seen following power law (1.1) for several decades.

To study the long-time dependence of the coarsening rate on the drop shape, we first choose an appropriate time scale. We are interested in times when the average drop has the mesa shape (2.17). Examining Eq. (3.3a), we see that the appropriate time scale must account for values of $Q$, $C_q$, and $J$ in the range of mesa drops. For these drops, Eq. (2.21b) suggests scaling $Q$ by $\alpha \bar{m}_0$, Eq. (3.6) shows that $C_q(Q)$ scales similar to $\alpha$, and $J$ scales similar to the drop separation $\ell$. Taken together, this motivates the choice of time scale

$$\tau = t/T \quad \text{where} \quad T = \frac{1}{\alpha^2 \mathbb{K}}. \tag{4.2}$$

The limit $\alpha \to 0$ forces $T \to \infty$. Hence the time scale $T$ describes when the remaining array is dominated by mesalike drops and slowed coarsening occurs. It may be very long if $\alpha$ is small. In fact, if $\alpha M_c < 1$ then all coarsening will follow (1.1) leading to a single final parabolic drop. We will focus attention on the behavior of the other case, $\alpha M_c > 1$, for the remainder of this section. Note that this also implies that $T$ alone cannot predict the onset of slow coarsening; the transition also depends on the value of $\alpha M_c$.

Using the new time $\tau$, our simulations show the self-similar structure of the coarsening. From the data used for Fig. 12, we observe that

$$\bar{Q}(\tau) \approx -1.33 \ln \tau, \tag{4.3}$$

see Fig. 14, where the value 1.33 was obtained from a one-parameter numerical fit. Using the fact that the total core mass $M_c$ is effectively constant, we can write

$$N(\tau;\alpha) = \frac{\bar{m}_0}{\bar{m}(\tau)} N_0, \tag{4.4}$$

where $\bar{m}(\tau)$ is the current mean droplet mass. The dynamics of $\bar{m}(\tau)$ can then be found by using Eq. (2.21b) and replacing $Q$ by $\bar{Q}(\tau)$. Doing this gives

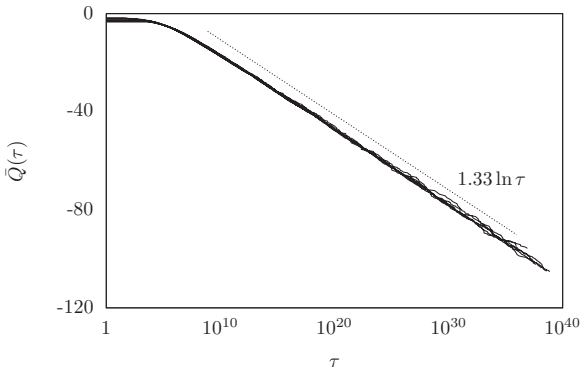


FIG. 14. The mean logarithmic excess pressure $\bar{Q}$ versus $\tau$ for the simulations shown in Fig. 12. The dashed line shows the apparent behavior.

$$\bar{m}(\tau) \approx \frac{1}{\sqrt{3}\alpha}\left(1.33 \ln \tau + \frac{1}{2} \ln \alpha\right). \tag{4.5}$$

Using Eq. (4.4),

$$N(\tau) \approx \frac{\sqrt{3}\alpha M_c}{1.33 \ln \tau + \frac{1}{2} \ln \alpha}, \tag{4.6}$$

where the $\frac{1}{2} \ln \alpha$ term acts to scale onset times. This motivates the relationship

$$N(\tau) \propto \frac{\alpha \bar{m}_0}{\ln \tau} N_0 \quad \text{for } \tau \to \infty, \tag{4.7}$$

see Fig. 15. Instead of a power law, this is a slow inverse-logarithmic decay of $N$. In terms of the mesa parameter, we see that this is equivalent to $\alpha \bar{m}_0 N_0 / N = \bar{\mathbb{M}}(\tau)$, where $\bar{\mathbb{M}} \propto \ln \tau$ is the mean dynamic mesa parameter. Thus increasing either $\alpha$ or $\bar{m}_0$ increases the initial $\bar{\mathbb{M}}$, causing slower coarsening to begin earlier.

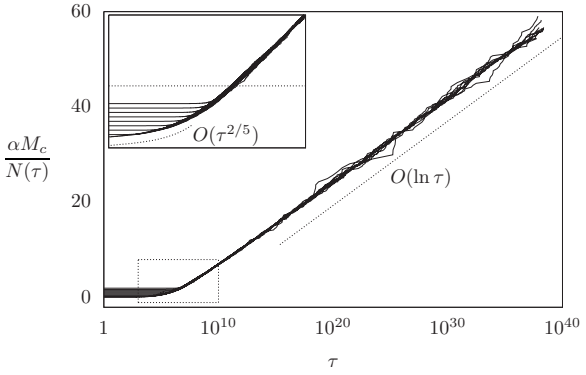


FIG. 15. The same data as in Fig. 13 plotted using $\alpha M_c / N$ versus $\tau$. The dotted line is the prediction (4.7) for long times. The boxed region is shown enlarged in the inset; the horizontal dotted line divides mesalike behavior and paraboliclike behavior, corresponding to $\bar{\mathbb{M}}$ being large. Below this line, the power law for parabolic drops can be seen.

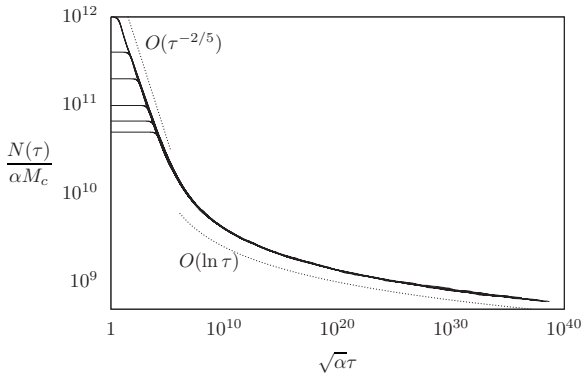


FIG. 16. The data of both Figs. 12 and 13 replotted using $N/(\alpha M_c)$ against $\sqrt{\alpha}\tau$. All curves collapse onto a single trend that follows the parabolic drop power law for short times and the mesa drop logarithmic law for long times (both shown dashed).

Replotting the data in Fig. 13 with $\alpha M_c/N$ versus $\tau$ (Fig. 15) shows that all of the curves collapse onto a single line as described by Eq. (4.6). The inset shows an enlargement of the boxed early-time portion. The transition from the power law to the logarithmic law occurs on either side of the dotted horizontal line representing $\bar{\mathbb{M}}$ being large.

It is also illustrative to plot $N/(\alpha M_c)$ against $\sqrt{\alpha}\tau$ on a log-log plot, as in Fig. 16 where all of the data in Fig. 12 and Fig. 13 are replotted. This shows the relationship (4.7) collapses all curves into a single trend. Short times experience the parabolic drop related power law, while long times display the mesa drop related logarithmic law.

## V. SUMMARY AND CONCLUSIONS

We have described the coarsening dynamics of an idealized one-dimensional thin film with the wetting potential modified by the inclusion of gravity. While the influence of gravity is negligible in the early stages of evolution, coarsening dynamics leads to the formation of drops with much larger height scales. Hence gravity will eventually come into play with the crossover described in terms of the mesa parameter $\mathbb{M}$. Large drops with $\mathbb{M}>1$ are "mesalike" being much wider and flatter than smaller parabolic drops with $\mathbb{M} \ll 1$.

The presence of gravity has been to shown to dramatically slow the rate of coarsening from the $N(t) \propto t^{-2/5}$ power law for parabolic drops. As coarsening proceeds, the average drop mass grows, and provided there is sufficient total mass in the system, eventually makes the mean dynamic parameter value large, $\bar{\mathbb{M}}(t) \gg 1$. In this long-time regime, the system is dominated by a large population of mesa drops which coarsen according to the slower logarithmic law (4.7) coarsening rate. Some studies comment on the transition to this behavior [26], but due to the time scales involved it is difficult to reach in experiments and due to limitations in computational power, direct simulations of Eq. (1.13) in one and two dimensions have been limited to systems of tens or hundreds of drops [23,24,26]. Our reduction of the PDE to a coarsening system (3.3) has allowed us to obtain much clearer statistical trends based on much larger systems.

Many new questions have been opened up and much further work is needed on coarsening in thin films. In order to connect to real experimental systems, extensions of the analysis and simulations to two dimensions are needed. Some primarily theoretical results suggest that qualitatively similar behavior should hold [14]. Other limits including that of "dense" droplet arrays and cases where collisions dominate the coarsening process are also likely to have interesting interactions with the influence of gravity. Analyses for experiments with timescales that might allow for these coarsening regimes to be observed (with destabilizing gravitational influences [39–41] or coarsening with condensation [27,42]) are also very important future directions.

## ACKNOWLEDGMENTS

This research was supported by NSF DMS Grant Nos. 0244498 FRG and 0239125 CAREER.

[1] V. M. Starov, M. G. Velarde, and C. J. Radke, *Wetting and Spreading Dynamics* (CRC Press, Boca Raton, FL, 2007).
[2] A. Oron, S. H. Davis, and S. G. Bankoff, Rev. Mod. Phys. **69**, 931 (1997).
[3] W. W. Zhang and J. R. Lister, Phys. Fluids **11**, 2454 (1999).
[4] M. B. Williams and S. H. Davis, J. Colloid Interface Sci. **90**, 220 (1982).
[5] A. L. Bertozzi, G. Grün, and T. P. Witelski, Nonlinearity **14**, 1569 (2001).
[6] T. P. Witelski and A. J. Bernoff, Physica D **147**, 155 (2000).
[7] G. Reiter, Phys. Rev. Lett. **68**, 75 (1992).
[8] G. Reiter, A. Sharma, A. Casoli, M.-O. David, R. Khanna, and P. Auroy, Langmuir **15**, 2551 (1999).
[9] S. Herminghaus, K. Jacobs, K. Mecke, J. Bischof, A. Fery, M. Ibn-Elhaj, and S. Schlagowski, Science **282**, 916 (1998).
[10] J. Bischof, D. Scherer, S. Herminghaus, and P. Leiderer, Phys. Rev. Lett. **77**, 1536 (1996).
[11] R. Seemann, S. Herminghaus, and K. Jacobs, Phys. Rev. Lett. **86**, 5534 (2001).
[12] K. B. Glasner and T. P. Witelski, Phys. Rev. E **67**, 016302 (2003).
[13] K. Glasner and T. Witelski, Physica D **209**, 80 (2005).
[14] F. Otto, T. Rump, and D. Slepčev, SIAM J. Math. Anal. **38**, 503 (2006).
[15] R. Limary and P. F. Green, Langmuir **19**, 2419 (2003).
[16] P. de Gennes, Rev. Mod. Phys. **57**, 827 (1985).
[17] F. Brochard-Wyart, H. Hervet, C. Redon, and F. Rondelez, J. Colloid Interface Sci. **142**, 518 (1991).
[18] P.-G. de Gennes, F. Brochard-Wyart, and D. Quere, *Capillarity and wetting phenomena: drops, bubbles, pearls, waves* (Springer Verlag, New York, 2003).
[19] S. Herminghaus and F. Brochard, C. R. Phys. **7**, 1073 (2006).

[20] J. Becker, G. Grün, R. Seemann, H. Mantz, K. Jacobs, K. Mecke, and R. Blossey, Nat. Mater. **2**, 59 (2003).
[21] J. A. Diez and L. Kondic, Phys. Fluids **19**, 072107 (2007).
[22] U. Thiele, M. G. Velarde, K. Neuffer, and Y. Pomeau, Phys. Rev. E **64**, 031602 (2001).
[23] S. Saprykin, P. M. J. Trevelyan, R. J. Koopmans, and S. Kalliadasis, Phys. Rev. E **75**, 026306 (2007).
[24] A. Sharma and R. Verma, Langmuir **20**, 10337 (2004).
[25] V. S. Mitlin, J. Colloid Interface Sci. **156**, 491 (1993).
[26] L. S. Fisher and A. A. Golovin, J. Colloid Interface Sci. **291**, 515 (2005).
[27] A. Oron and S. G. Bankoff, Phys. Fluids **13**, 1107 (2001).
[28] V. S. Mitlin and N. V. Petviashvili, Phys. Lett. A **192**, 323 (1994).
[29] V. S. Mitlin, J. Colloid Interface Sci. **227**, 371 (2000).
[30] L. W. Schwartz, R. V. Roy, R. R. Eley, and S. Petrash, J. Colloid Interface Sci. **234**, 363 (2001).
[31] L. W. Schwartz, in *Free Surface Flows with Viscosity* (Computational Mechanics Publications, Boston, 1997), pp. 203–233.
[32] C. Neto, K. Jacobs, R. Seemann, R. Blossey, J. Becker, and G. Grün, J. Phys.: Condens. Matter **15**, S421 (2003).
[33] F. Brochard-Wyart, J.-M. di Meglio, D. Quere, and P. de Gennes, Langmuir **7**, 335 (1991).
[34] L. Leger and J. F. Joanny, Rep. Prog. Phys. **55**, 431 (1992).
[35] A. Martin, O. Rossier, A. Buguin, P. Auroy, and F. Brochard-Wyart, Eur. Phys. J. E **3**, 337 (2000).
[36] K. B. Glasner, Phys. Fluids **15**, 1837 (2003).
[37] E. K. O. Hellen and J. Krug, Phys. Rev. E **66**, 011304 (2002).
[38] S. Watson, F. Otto, B. Rubinstein, and S. Davis, Physica D **178**, 127 (2003).
[39] L. Limat, F. Giorgiutti, M. F. P. Jenffer, and J.-E. Wesfreid, Rev. Gen. Therm. **36**, 672 (1997).
[40] J. R. de Bruyn, Phys. Fluids **9**, 1599 (1997).
[41] L. Limat, P. Jenffer, B. Dagens, E. Touron, M. Fermigier, and J.-E. Wesfreid, Physica D **61**, 166 (1992).
[42] D. Beysens, C. R. Phys. **7**, 1082 (2006).